arXiv:0704.0407v1 [nucl-th] 3 Apr 2007

Density dependent hadronic models and the relation between neutron stars and neutron skin thickness

S.S. Avancini,[1] J.R. Marinelli,[1] D.P. Menezes,[1] M.M.W. Moraes,[1] and C. Providência[2]

[1] *Depto de Física - CFM - Universidade Federal de Santa Catarina Florianópolis - SC - CP. 476 - CEP 88.040 - 900 - Brazil*
[2] *Centro de Física Teórica - Dep. de Física - Universidade de Coimbra - P-3004 - 516 - Coimbra - Portugal*

In the present work we investigate the main differences in the lead neutron skin thickness, binding energy, surface energy and density profiles obtained with two different density dependent hadron models. Our results are calculated within the Thomas-Fermi approximation with two different numerical prescriptions and compared with results obtained with a common parametrization of the non-linear Walecka model. The neutron skin thickness is a reflex of the equation of state properties. Hence, a direct correlation between the neutron skin thickness and the slope of the symmetry energy is found. We show that within the present approximations the asymmetry parameter for low momentum transfer polarized electron scattering is not sensitive to the model differences.

PACS number(s): 21.65.+f,24.10.Jv,95.30.Tg,26.60.+c

I. INTRODUCTION

The relation between neutron star properties which are obtained from adequate equations of state (EoS) and the neutron skin thickness has long been a topic of investigation in the literature. The details of this relation and the important quantities to be discussed have been well established in [1], where it was shown that the difference between the neutron and the proton radii, the neutron skin thickness, is linearly correlated with the pressure of neutron matter at sub-nuclear densities. This is so because the properties of neutron stars are obtained from appropriate EoS whose symmetry energy depends on the density and also controls the size of the neutron skin thickness in heavy and asymmetric nuclei, as ^{208} Pb, for instance. It is important to remember that the EoS in neutron stars is also very isospin asymmetric due to the β- equilibrium constraint.

Hence, isospin asymmetry plays a major role in the understanding of the density dependence of the symmetry energy and the consequences it may arise [2]. In [3, 4] it was shown that the models that yield smaller neutron skins in heavy nuclei tend to yield smaller neutron star radii due to a softer EoS.

Neutron stars are believed to have a solid crust formed by nonuniform neutron rich matter in β-equilibrium above a liquid mantle. In the inner crust nuclei coexist with a gas of neutrons which have dripped out. The properties of this crust as, for instance, its thickness and pressure at the crust-core interface depend a lot on the density dependence of the EoS used to describe it [4, 5]. On the other hand, it is well known [6, 7] that the existence of phase transitions from liquid to gas phases in asymmetric nuclear matter (ANM) is intrinsically related with the instability regions which are limited by the spinodals. Instabilities in ANM described within relativistic mean field hadron models, both with constant and density dependent couplings at zero and finite temperatures have already been investigated [7] and it was shown that the main differences occur at finite temperature and large isospin asymmetry close to the boundary of the instability regions. In neutral neutron-proton-electron (npe) matter the electrons are also included. In a thermodynamical calculation the instabilities almost completely disappear due to the high electron Fermi energy [8].

However, in a dynamical calculation which includes the Coulomb interaction and allows for independent neutron, proton and electron fluctuations [9, 10], it is seen that the electron dynamics tends to restore the short wavelength instabilities although moderated by the high electron Fermi energy.

Moreover, it is also known that the liquid-gas phase transition in ANM can lead to an isospin distillation phenomenon, characterized by a larger proton fraction in the liquid phase than in the gas phase. This is due to the repulsive isovector channel of the nuclear interaction [11, 12, 13].

In a recent work the spinodal section and related quantities, as the neutron to proton density fluctuations responsible for the distillation effect, has been studied within different relativistic models [8]. It was shown that the distillation effect within density dependent relativistic models decreases with density above a nuclear density of $\sim 0.02-0.03\,\mathrm{fm}^{-3}$, a result similar to the one obtained with the SLy230a parametrization of Skyrme interaction [14] and contrary to the results found with the more common relativistic parametrizations with no density dependent coupling parameters. In the last case the distillation effect becomes always larger as the density increases.

Also, the behavior of the symmetry energy obtained with density dependent models is closer to what one obtains with non-relativistic models than with other relativistic models with constant couplings [7]. In an attempt to understand this behavior, a comparison between the non-relativistic Skyrme effective force and relativistic mean field models at subsaturation densities was performed [15]. It was shown that the relativistic models could also be reduced to an energy density functional similar to the one describing the Skyrme interaction.

There have already been some efforts in order to compare nuclear matter and finite nuclei properties obtained both with relativistic and non-relativistic models [16, 17] but there is no clear or obvious explanations for the differences. At very low densities both, the relativistic and the non-relativistic approaches predict a non-homogeneous phase commonly named *pasta phase*, formed by a competition between the long-range Coulomb repulsion and the short-range nuclear attraction [18].

Based on the above arguments, it is very important that an accurate experimental measurement of the neutron skin thickness is achieved. This depends on a precise measurement of both the charge and the neutron radius. The charge radius is already known within a precision of one percent for most stable nuclei, using the well-known single-arm and non-polarized elastic electron scattering technique as well as the spectroscopy of muonic atoms [19] . For the neutron radius, our present knowledge has an uncertainty of about 0.2 fm [20]. However, using polarized electron beams it is possible to obtain the neutron distribution in nuclei in a fairly model independent way, as first discussed in [21] and, as a consequence, to obtain the desired neutron radius. In fact, the Parity Radius Experiment (PREX) at the Jefferson Laboratory [22] is currently running to measure the ^{208}Pb neutron radius with an accuracy of less than 0.05 fm, using polarized electron scattering.

In the present work, we use two different hadronic models that incorporate density dependence in different ways. The first one, to which we refer next as the TW model is a density dependent hadronic model with the meson-to-nucleon couplings explicitly dependent of the density [23, 24]. In the following it is used to calculate the neutron skin thickness of ^{208}Pb, which is a neutron-rich heavy nucleus. This model was chosen because it is based on a microscopic calculation, fits well many nuclei properties and, as stated above, has shown to provide results which are different from the usual NL3 [25] and TM1 [26] parametrizations for the non-linear Walecka model (NLWM), having a richer density dependence of the symmetry energy than most of the relativistic nuclear models. The original motivation for the development of this density dependent hadronic model [27, 28] was to reproduce results obtained with the relativistic Dirac-Brueckner Hartree-Fock (DBHF) theory [29]. Later the DBHF calculations for nuclear matter were taken only as a guide for a suitable parametrization of the density dependence of the meson-nucleon coupling operators [24, 30]. Moreover, density dependent hadronic models can also be a useful tool in obtaining EoS for neutron stars even if hyperons are to be considered [32], which is not the case if NL3 or TM1 are used. Both, NL3 and TM1, can only be used if the EoS is restricted to accommodate neutrons, protons and the leptons necessary to enforce β-stability. Once hyperons are included, the nucleons acquire a negative effective mass above $\sim 3-4\rho_0$ densities [33, 34], where ρ_0 is the nuclear saturation density.

The second model, that we refer to as NL$\omega\rho$ model, includes non-linear $\sigma-\rho$ and $\omega-\rho$ couplings [3, 35, 36, 37] which allow to change the density dependence of the symmetry energy of the most common parametrizations of the NLWM that show essentially a linear behavior of the symmetry energy with density. However, the symmetry energy determines the behavior of isospin asymmetric matter and therefore is intrinsically related to the characteristics of the EoS that can describe neutron stars. Within this model the authors of [3] have shown that the neutron skin thickness of ^{208}Pb was sensitive to the isovector channel of the nuclear interaction and there was a correlation between neutron skin thickness of nuclei and properties of neutron stars.

For the sake of completeness, the results of the present work, whenever possible are compared with the results obtained with the NL3 parametrization of the NLWM, known to describe finite nuclei properties well.

We perform two different numerical calculations to obtain the ^{208}Pb properties: a Thomas-Fermi approximation based on the liquid-gas phase transition developed in [38] and a Thomas-Fermi approximation based on a method proposed in [39], where a harmonic oscillator basis is used. We restrict ourselves to the Thomas-Fermi approximation because, as we show in the Results section at the end of the paper, for the purpose of obtaining correct surface energy and neutron-skin thickness, it is almost as good as the solution of the Dirac equation.

At this point it is worth mentioning that the scalar-isovector δ mesons, which play an important role in the isospin channel, could also be incorporated in our work as done in [7, 9, 40] but in order to make the comparisons among different approximations as simple as possible, they will be included in a future work. Finally, as we are interested in nuclei ground state properties, all calculations are performed at zero temperature.

II. THE TW DENSITY DEPENDENT HADRONIC MODEL

Next we describe the main quantities of the TW model, which has density dependent coupling parameters. The Lagrangian density reads:

$$\mathcal{L} = \bar{\psi}\left[\gamma_\mu\left(i\partial^\mu - \Gamma_v V^\mu - \frac{\Gamma_\rho}{2}\boldsymbol{\tau}\cdot\mathbf{b}^\mu\right.\right.$$

$$\left.\left. -e\frac{(1+\tau_{i3})}{2}A^\mu\right) - (M - \Gamma_s\phi)\right]\psi$$

$$+\frac{1}{2}(\partial_\mu\phi\partial^\mu\phi - m_s^2\phi^2) - \frac{1}{4}\Omega_{\mu\nu}\Omega^{\mu\nu}$$

$$+\frac{1}{2}m_v^2 V_\mu V^\mu - \frac{1}{4}\mathbf{B}_{\mu\nu}\cdot\mathbf{B}^{\mu\nu} + \frac{1}{2}m_\rho^2\mathbf{b}_\mu\cdot\mathbf{b}^\mu - \frac{1}{4}F_{\mu\nu}F^{\mu\nu} \quad (1)$$

where ϕ, V^μ, $\mathbf{b}^\mu$ and A^μ are the scalar-isoscalar, vector-isoscalar and vector-isovector meson fields and the photon field respectively, $\Omega_{\mu\nu} = \partial_\mu V_\nu - \partial_\nu V_\mu$, $\mathbf{B}_{\mu\nu} = \partial_\mu \mathbf{b}_\nu - \partial_\nu \mathbf{b}_\mu - \Gamma_\rho(\mathbf{b}_\mu \times \mathbf{b}_\nu)$, $F_{\mu\nu} = \partial_\mu A_\nu - \partial_\nu A_\mu$ and $\tau_{p3} = 1$, and $\tau_{n3} = -1$. The parameters of the model are: the nucleon mass $M = 939$ MeV, the masses of the mesons m_s, m_v, m_ρ, the electromagnetic coupling constant $e = \sqrt{4\pi/137}$ and the density dependent coupling constants Γ_s, Γ_v and Γ_ρ, which are adjusted in order to reproduce some of the nuclear matter bulk properties shown in Table I, using the following parametrization:

$$\Gamma_i(\rho) = \Gamma_i(\rho_{sat}) h_i(x), \quad x = \rho/\rho_{sat}, \tag{2}$$

with

$$h_i(x) = a_i \frac{1 + b_i(x + d_i)^2}{1 + c_i(x + d_i)^2}, \quad i = s, v \tag{3}$$

and

$$h_\rho(x) = \exp[-a_\rho(x - 1)], \tag{4}$$

with the values of the parameters m_i, $\Gamma_i(\rho_{sat})$, a_i, b_i, c_i and d_i, $i = s, v, \rho$ given in [24]. This model does not include self-interaction terms for the meson fields (i.e. $\kappa = 0$, $\lambda = 0$ and $\xi = 0$) as in NL3 or TM1 parametrizations for the NLWM.

The field equations of motion follow from the Euler-Lagrange equations. When they are obtained, some care has to be taken since the coupling operators depend on the baryon fields $\bar\psi$ and ψ through the density. When the partial derivatives of $\mathcal{L}$ are performed relatively to the fields $\bar\psi$ and ψ, they yield extra terms due to the functional dependence of the coupling operators. The new terms are absent in the usual Quantum Hadrodynamic (QHD, NLWM) models [25, 26, 31]. The equations of motion for the fields read:

$$\begin{aligned}
(\partial_\mu \partial^\mu + m_\phi^2)\phi &= \Gamma_s \bar\psi\psi, && (5)\\
\partial_\nu \Omega^{\mu\nu} + m_v^2 V^\mu &= \Gamma_v \bar\psi \gamma^\mu \psi, && (6)\\
\partial_\nu \mathbf{B}^{\ \mu\nu} + m_\rho^2 \mathbf{b}^\mu &= \frac{\Gamma_\rho}{2} \bar\psi \boldsymbol{\tau} \gamma^\mu \psi, && (7)\\
\partial_\nu F^{\mu\nu} &= \frac{e}{2} \bar\psi (1 + \tau_3) \gamma^\mu \psi, && (8)\\
\left[\gamma_\mu (i\partial^\mu - \Sigma^\mu) - M^*\right] \psi &= 0 \ , && (9)
\end{aligned}$$

where $M^* = M - \Gamma_s \phi$. Notice that in the equation of motion for the baryon field ψ the vector self-energy consists of two terms, $\Sigma_\mu = \Sigma_\mu^{(0)} + \Sigma_\mu^R$, where:

$$\Sigma_\mu^{(0)} = \Gamma_\omega V_\mu + \frac{\Gamma_\rho}{2} \boldsymbol{\tau} \cdot \mathbf{b}_\mu + \frac{e}{2}(1 + \tau_3) A_\mu, \tag{10}$$

$$\Sigma_\mu^R = \left(\frac{\partial \Gamma_v}{\partial \rho} V^\nu j_\nu + \frac{1}{2} \frac{\partial \Gamma_\rho}{\partial \rho} \mathbf{b}_\nu \cdot \mathbf{j}_3^\nu - \frac{\partial \Gamma_\phi}{\partial \rho} \bar\psi \psi \phi \right) u_\mu \ , \tag{11}$$

where $\Sigma_\mu^{(0)}$ is the usual vector self-energy, $\hat\rho u_\mu = j_\mu$ with $u^2 = 1$ $j_\nu = \bar\psi \gamma_\nu \psi$, $\mathbf{j}_3^\nu = \bar\psi \boldsymbol{\tau} \gamma^\nu \psi$ and, as a result of the derivative of the Lagrangian with respect to ρ a new term appears, Σ_μ^R, which is called rearrangement self-energy and has been shown to play an essential rôle in the applications of the theory. This term guarantees the thermodynamical consistency and the energy-momentum conservation. For more detailed calculations, at zero and finite temperatures, please refer to [41].

In the static case there are no currents in the nucleus and the spatial vector components are zero. Therefore, the mesonic equations of motion become:

$$\nabla^2 \phi = m_s^2 \phi - \Gamma_s \rho_s, \tag{12}$$

$$\nabla^2 V_0 = m_v^2 V_0 - \Gamma_v \rho, \tag{13}$$

$$\nabla^2 b_0 = m_\rho^2 b_0 - \frac{\Gamma_\rho}{2} \rho_3, \tag{14}$$

$$\nabla^2 A_0 = -e \rho_p, \tag{15}$$

where $\rho_s =< \bar\psi\psi >$ is the scalar density, $\rho = \rho_p + \rho_n$, $\rho_3 = \rho_p - \rho_n$ and ρ_p and ρ_n are the proton and neutron densities.

A. Thomas-Fermi approximation

We first define the functional

$$\Omega = E - \mu_p B_p - \mu_n B_n, \tag{16}$$

where E is the energy, μ_p (μ_n) is the proton (neutron) chemical potential and B_p (B_n) is the proton (neutron) number. Within the semi-classical Thomas-Fermi approximation, the energy of the nuclear system with particles described by the one-body phase-space distribution function $f(\mathbf{r}, \mathbf{p}, t)$ at position $\mathbf{r}$, instant t with momentum $\mathbf{p}$ is given by

$$\begin{aligned}
E = \sum_i \gamma \int \mathrm{d}^3 r \frac{\mathrm{d}^3 p}{(2\pi)^3} f_i(\mathbf{r}, \mathbf{p}, t) \left(\sqrt{\mathbf{p}^2 + M^{*2}} + \mathcal{V}_i \right) \\
+ \frac{1}{2} \int \mathrm{d}^3 r \left[(\nabla\phi)^2 + m_s^2 \phi^2 - (\nabla V_0)^2 - m_v^2 V_0^2 \right. \\
\left. - (\nabla b_0)^2 - m_\rho^2 b_0^2 - (\nabla A_0)^2 \right] \qquad (17)
\end{aligned}$$

where

$$\mathcal{V}_p = \Gamma_v V_0 + \frac{\Gamma_\rho}{2} b_0 + e A_0 \ , \quad \mathcal{V}_n = \Gamma_v V_0 - \frac{\Gamma_\rho}{2} b_0 \ ,$$

$\gamma = 2$ refers to the spin multiplicity and the distribution functions for protons and neutrons are

$$f_i = \theta(k_{Fi}^2(r) - p^2), \qquad i = p, n \ .$$

In this approach, the scalar, proton and neutron densities become:

$$\rho_s(r) = \frac{\gamma}{2\pi^2}\sum_{i=p,n}\int_0^{k_{Fi}(r)} p^2 \mathrm{d}p \frac{M^*}{\epsilon}$$

with $\epsilon = \sqrt{p^2 + M^{*2}}$ and

$$B_i = \int \mathrm{d}^3 r \rho_i, \quad \rho_i(r) = \frac{\gamma}{6\pi^2} k_{Fi}^3(r).$$

From the above expressions we get for (16)

$$\Omega = \int \mathrm{d}^3 r \left(\frac{1}{2}\left[(\nabla\phi)^2 - (\nabla V_0)^2 - (\nabla b_0)^2 - (\nabla A_0)^2\right] + V_{ef} \right)$$

with

$$V_{ef} = \frac{1}{2}\left[m_s^2\phi^2 - m_v^2 V_0^2 - m_\rho^2 b_0^2\right] - \mu_p\rho_p - \mu_n\rho_n$$

$$+ \frac{\gamma}{2\pi^2}\sum_{i=p,n}\int_0^{k_{Fi}} \mathrm{d}p p^2 \epsilon + \Gamma_v V_0 \rho + \Gamma_\rho \frac{b_0}{2}\rho_3 + e A_0 \rho_p \quad (18)$$

Minimization of Ω with respect to $k_{Fi}(r)$, $i = p, n$, gives rise to the following conditions

$$k_{Fp}^2 \left(\mu_p - \sqrt{k_{Fp}^2 + M^{*2}} - \Gamma_v V_0 - \frac{\Gamma_\rho}{2} b_0 - e A_0 - \Sigma_0^R \right) = 0$$

and

$$k_{Fn}^2 \left(\mu_n - \sqrt{k_{Fn}^2 + M^{*2}} - \Gamma_v V_0 + \frac{\Gamma_\rho}{2} b_0 - \Sigma_0^R \right) = 0,$$

where the rearrangement term is

$$\Sigma_0^R = \frac{\partial\,\Gamma_v}{\partial\rho}\,\rho\, V_0 + \frac{\partial\,\Gamma_\rho}{\partial\rho}\,\rho_3\,\frac{b_0}{2} - \frac{\partial\,\Gamma_s}{\partial\rho}\,\rho_s\,\phi.$$

From the above equations we obtain $k_{Fp} = 0$ and $k_{Fn} = 0$ or, for k_{Fp} or k_{Fn} different from zero,

$$\mu_p = \sqrt{k_{Fp}^2 + M^{*2}} + \Gamma_v V_0 + \frac{\Gamma_\rho}{2} b_0 + e A_0 + \Sigma_0^R, \quad (19)$$

$$\mu_n = \sqrt{k_{Fn}^2 + M^{*2}} + \Gamma_v V_0 - \frac{\Gamma_\rho}{2} b_0 + \Sigma_0^R. \quad (20)$$

The values of k_{Fp} and k_{Fn} are obtained inverting these two last equations.

Such density dependences in the coupling parameters do not affect the energy functional but of course affect its derivative such as the pressure density and the chemical potentials. As already discussed in the literature [7, 8, 9, 32], the rearrangement term is crucial in obtaining different behaviors in physical properties related to the chemical potentials or to their derivatives with respect to the density, such as spinodal regions, as compared with the more common NL3 or TM1 parametrizations.

III. NL$\omega\rho$ MODEL

The Lagrangian density that incorporates the extra non-linear $\sigma - \rho$ and $\omega - \rho$ couplings [3, 35, 36, 37] reads

$$\mathcal{L} = \bar{\psi}\Big[\gamma_\mu\Big(i\partial^\mu - g_v V^\mu - \frac{g_\rho}{2}\boldsymbol{\tau}\cdot\mathbf{b}^\mu$$

$$-e\frac{(1+\tau_{i3})}{2}A^\mu\Big) - (M - g_s\phi)\Big]\psi$$

$$+\frac{1}{2}(\partial_\mu\phi\partial^\mu\phi - m_s^2\phi^2) - \frac{1}{3!}\kappa\phi^3 - \frac{1}{4!}\lambda\phi^4 - \frac{1}{4}\Omega_{\mu\nu}\Omega^{\mu\nu}$$

$$+\frac{1}{2}m_v^2 V_\mu V^\mu - \frac{1}{4}\mathbf{B}_{\mu\nu}\cdot\mathbf{B}^{\mu\nu} + \frac{1}{2}m_\rho^2\mathbf{b}_\mu\cdot\mathbf{b}^\mu - \frac{1}{4}F_{\mu\nu}F^{\mu\nu}$$

$$+ g_\rho^2\mathbf{b}_\mu\cdot\mathbf{b}^\mu[\Lambda_s g_s^2\phi^2 + \Lambda_v g_v^2 V_\mu V^\mu], \quad (21)$$

where $\Omega_{\mu\nu}$, $\mathbf{B}_{\mu\nu}$ and $F_{\mu\nu}$ are defined after eq.(1). The parameters of the model are again the masses and the couplings, which are now constants, i.e., g_s replaces Γ_s, g_v replaces Γ_v and g_ρ replaces Γ_ρ. Non-linear σ terms are also included. We have followed the prescription of [3], where the starting point was the NL3 parametrization and the g_ρ coupling was adjusted for each value of the coupling Λ_i studied in such a way that for $k_F = 1.15$ fm^{-1} (not the saturation point) the symmetry energy is 25.68 MeV. In the present work we set $\Lambda_s = 0$ as in [37]. Notice that other possibilities for this model with $\sigma - \rho$ and $\omega - \rho$ couplings have already been discussed in the literature as in [4], for instance.

The mesonic equations of motion in the Thomas-Fermi approximation become

$$\nabla^2\phi = m_s^2\phi - g_s\rho_s + \frac{\kappa}{2}\phi^2 + \frac{\lambda}{6}\phi^3 \quad (22)$$

$$\nabla^2 V_0 = m_v^2 V_0 - g_v\rho + 2\Lambda_v g_v^2\, V_0\, g_\rho^2 b_0^2, \quad (23)$$

$$\nabla^2 b_0 = m_\rho^2 b_0 - \frac{g_\rho}{2}\rho_3 + 2\Lambda_v g_\rho^2 b_0 g_v^2 V_0^2, \quad (24)$$

$$\nabla^2 A_0 = -e\rho_p, \quad (25)$$

and the expression for the energy reads

$$E = \sum_i \int \mathrm{d}^3 r \Big(\gamma \int_0^{k_{Fi}(r)} \frac{\mathrm{d}^3 p}{(2\pi)^3}\sqrt{\mathbf{p}^2 + M^{*2}}$$

$$+\frac{1}{2}\big[(\nabla\phi)^2 + m_s^2\phi^2 - (\nabla V_0)^2 - m_v^2 V_0^2$$

$$-(\nabla b_0)^2 - m_\rho^2 b_0^2 - (\nabla A_0)^2$$

$$+g_v V_0 \rho + \frac{g_\rho}{2}\rho_3 b_0 + eA_0\rho_p\Big]$$

$$+\frac{\kappa}{6}\phi^3 + \frac{\lambda}{24}\phi^4 - \Lambda_v g_v^2 V_0^2 g_\rho^2 b_0^2\Big) . \tag{26}$$

All other expressions are very similar to the ones obtained from the TW model and can be read off from them bearing in mind that the density dependent couplings have to be replaced by the constant couplings. In particular the chemical potentials do not contain the rearrangement term Σ_0^R.

IV. NUMERICAL RESULT VIA A NUCLEATION PROCESS

At this point, eqs. (12-15) for the TW model and eqs. (22-25) for the NL$\omega\rho$ model have to be solved numerically in a self-consistent way and hence, initial and boundary conditions for each equation are necessary. One of the methods we use here is based on a prescription given in [38], where these conditions are obtained from a situation of phase coexistence in a mean field approximation with classical meson fields and no electromagnetic interaction. The method is well explained in [38] and, as we are using different models here, just the main equations are written next.

For the TW model, the equilibrium equations for homogeneous matter for the fields are:

$$m_s^2\phi - \Gamma_s\ \rho_s = 0, \tag{27}$$
$$m_v^2 V_0 - \Gamma_v\ \rho = 0, \tag{28}$$
$$m_\rho^2 b_0 - \frac{\Gamma_\rho}{2}\ \rho_3 = 0, \tag{29}$$

and for the energy and pressure density:

$$\mathcal{E} = \frac{1}{\pi^2}\sum_i \int_0^{k_{Fi}} p^2 dp\ \sqrt{\mathbf{p}^2 + M^{*2}}$$

$$+\frac{m_s^2}{2}\phi^2 + \frac{m_v^2}{2}V_0^2 + \frac{m_\rho^2}{2}b_0^2, \tag{30}$$

$$P = \frac{1}{3\pi^2}\sum_i \int_0^{k_{Fi}} \frac{p^4 dp}{\epsilon} - \frac{m_s^2}{2}\phi^2 + \frac{m_v^2}{2}V_0^2 + \frac{m_\rho^2}{2}b_0^2$$

$$+\rho\Sigma_0^R. \tag{31}$$

For the NL$\omega\rho$ model, the equilibrium equations for homogenous matter, energy density and pressure become:

$$m_s^2\phi - g_s\rho_s + \frac{\kappa}{2}\phi^2 + \frac{\lambda}{6}\phi^3 = 0, \tag{32}$$

$$m_v^2 V_0 - g_v\rho + 2\Lambda_v g_v^2\, V_0\, g_\rho^2 b_0^2 = 0, \tag{33}$$

$$m_\rho^2 b_0 - \frac{g_\rho}{2}\rho_3 + 2\Lambda_v g_\rho^2 b_0 g_v^2 V_0^2 = 0, \tag{34}$$

$$\mathcal{E} = \frac{1}{\pi^2}\sum_i \int_0^{k_{Fi}} p^2 dp\sqrt{\mathbf{p}^2 + M^{*2}}$$

$$+\frac{1}{2}\left[m_s^2\phi^2 - m_v^2 V_0^2 - m_\rho^2 b_0^2\right] + g_v V_0\rho + \frac{g_\rho}{2}\rho_3 b_0$$

$$+\frac{\kappa}{6}\phi^3 + \frac{\lambda}{24}\phi^4 - \Lambda_v g_v^2 V_0^2 g_\rho^2 b_0^2. \tag{35}$$

and

$$P = \frac{1}{3\pi^2}\sum_i \int_0^{k_{Fi}} \frac{p^4 dp}{\epsilon} - \frac{m_s^2}{2}\phi^2 + \frac{m_v^2}{2}V_0^2 + \frac{m_\rho^2}{2}b_0^2$$

$$-\frac{\kappa}{6}\phi^3 - \frac{\lambda}{24}\phi^4 + \Lambda_v g_v^2 V_0^2 g_\rho^2 b_0^2. \tag{36}$$

Based on the geometrical construction and Gibbs conditions for phase coexistence, i.e., the pressure and both chemical potentials are equal in both phases, we build the binodal section given in Fig. 1. Notice that we have defined the proton fraction of the system as

$$y_p = \frac{\rho_p}{\rho}. \tag{37}$$

The binodal section yields the boundary conditions which we need. For the same pressure, two points, with different proton fractions are found. For each of these points, the meson fields and the densities are well defined and used as the initial and boundary conditions in eqs. (12-15), which are then solved. Once the meson fields are obtained, all the quantities that depend on them, as the energy, pressure densities, chemical potentials, baryonic densities, etc are also computed. The solution is a droplet with a certain proton fraction surrounded by a gas of neutrons. If stable nuclei are calculated, the gas vanishes because the energy of the system lies below the neutron drip line and the finite nuclei properties are easily calculated. This is the general method, but the results depend strongly on the model used because of the reasons discussed in Section VI.

V. NUMERICAL RESULT WITHIN A HARMONIC OSCILLATOR BASIS

Here a different prescription for solving the equations of motion and the thermodynamical quantities within the Thomas-Fermi approximation is used. According to [39], meson field equations of motion of the Klein-Gordon type with sources can be carried out by an expansion in a complete set of basis states. The harmonic oscillator functions with orbital angular momentum equal to zero are then chosen. The oscillator length is given by

$$b_B = \frac{b_0}{\sqrt{2}}, \quad b_0 = \sqrt{\frac{\hbar}{M\omega_0}}, \tag{38}$$

where M is the nucleon mass and ω_0 is the oscillator frequency. The meson fields and their corresponding inhomogeneous part can be expanded as

$$\Lambda(r) = \sum_{n=1}^{n_B} \Lambda_n R_{n0}(r), \quad S_\Lambda(r) = \sum_{n=1}^{n_B} S_n^\Lambda R_{n0}(r), \tag{39}$$

where $\Lambda(r) = \phi(r), V_0(r), b_0(r)$ and

$$R_{nl}(r) = \frac{N_{nl}}{b_0^{3/2}} x^l L_{n-1}^{l+1/2}(x^2) exp(-x^2/2), \tag{40}$$

where $x = r/b_0$ is the radius measured in units of the oscillator length,

$$N_{nl} = \sqrt{2(n-1)!/(l+n-1/2)!} \tag{41}$$

is the normalization constant and $L_n^m(x^2)$ are the associated Laguerre polynomials. For the calculation of the meson fields $l = 0$ in the expressions given below. Once the ansatz given by eqs.(39) are substituted into eqs.(12-14), a set of inhomogeneous equations is obtained:

$$\sum_{n'=1}^{n_B} \mathcal{H}_{nn'} \Lambda_{n'} = S_n^\Lambda \tag{42}$$

where

$$\mathcal{H}_{nn'} = \delta_{nn'} \left(b_B^{-2}(2(n-1) + 3/2) + m_\Lambda^2 \right)$$

$$+ \delta_{nn'+1} b_B^{-2} \sqrt{n(n+1/2)} + \delta_{n+1n'} b_B^{-2} \sqrt{n'(n'+1/2)}. \tag{43}$$

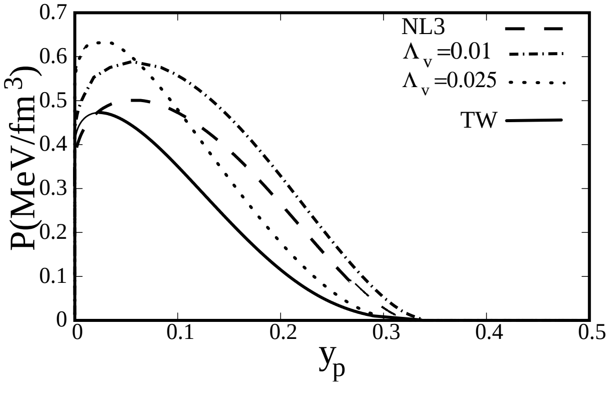

FIG. 1: Binodal section for the NL3, TW and NL$\omega\rho$ parametrizations.

Only the massive fields can be calculated with this method because the convergence of the Coulomb field, which has a long range, is very slow. The Green's function method is then chosen to describe the electromagnetic interaction:

$$A_0(r) = e \int r'^2 dr' \rho_p(r') G_c(r, r'), \tag{44}$$

with

$$G_c(r, r') = \begin{cases} 1/r & \text{for } r > r' \\ 1/r' & \text{for } r' > r. \end{cases} \tag{45}$$

VI. RESULTS

A. Parity Violating Electron Scattering and the Neutron Radius

We start this section by defining the asymmetry for polarized electron scattering of a hadronic target as

$$\mathcal{A} = \frac{d\sigma_+/d\Omega - d\sigma_-/d\Omega}{d\sigma_+/d\Omega + d\sigma_-/d\Omega}, \tag{46}$$

where $d\sigma_\pm/d\Omega$ is the differential cross section for initially polarized electrons with positive(+) and negative (−) helicities. As the electromagnetic interaction is not sensitive to the above difference, the asymmetry becomes dependent of the weak interaction between the electron and the target. Moreover, we know from the Standard Model that the neutral Z-boson couples more strongly to the neutron than to the proton. Those reasonings were then used in [21] to first propose a clean way to determine the neutron distribution in nuclei. If we consider elastic scattering on an even-even target nucleus, the asymmetry can be written in the form:

$$\mathcal{A} = \frac{Gq^2}{2\pi\alpha\sqrt{2}} a[\beta_V^p + \beta_V^n \frac{\rho_n(q)}{\rho_p(q)}]. \tag{47}$$

In the above expression, G, α, a and $\beta_V^{p,n}$ are Standard Model coupling constants as defined in [21], q is the transferred momentum by the electron to the nucleus and,

$$\rho_{n(p)}(q) = \int d^3r \; j_0(qr) \rho_{n(p)}(\mathbf{r}), \tag{48}$$

$\rho_{n(p)}(\mathbf{r})$ being the neutron (proton) distribution in configuration space and j_0 the spherical Bessel function of order zero. It is then clear that a small q measurement of the asymmetry gives the neutron radius of the distribution once the proton radius is well known. The proton and neutron mean-square radius are defined as

$$R_i^2 = \frac{\int d^3r r^2 \rho_i(\mathbf{r})}{\int d^3r \rho_i(\mathbf{r})}, \quad i = p, n. \tag{49}$$

The neutron skin thickness is defined as

$$\theta = R_n - R_p. \qquad (50)$$

In the PREX experiment mentioned in the Introduction, the asymmetry is expected to be measured at $q \approx 0.4\, fm^{-1}$ [22]. Also, because the target is a heavy nucleus (^{208}Pb), the above results for the asymmetry should be reconsidered for a detailed comparison with the experiment, since they were obtained using a Plane Wave Born Approximation for the electron [43]. For our present purposes, eq. (47) is sufficient to illustrate the sensitivity to the different model parametrizations and is used next in the presentation of our numerical results.

The surface energy per unit area of the droplets in the small surface thickness approximation, excluding the electromagnetic field, reads [38]

$$\sigma = \int_0^\infty \mathrm{d}r \left[\left(\frac{\mathrm{d}\phi}{\mathrm{d}r}\right)^2 - \left(\frac{\mathrm{d}V_0}{\mathrm{d}r}\right)^2 - \left(\frac{\mathrm{d}b_0}{\mathrm{d}r}\right)^2 \right]. \qquad (51)$$

However, as the electromagnetic interaction does not contribute to surface properties directly, we have kept the same definition for the surface energy.

In Table II we show the neutron and proton radius, the neutron skin thickness, the binding energy and the surface energy obtained within the Thomas-Fermi approximation and the two different numerical prescriptions described in the previous sections. All the results are sensitive to the numerical calculation although the analytical approximation is the same. When the nucleation method is performed, the neutron radius is systematically larger, what results in a thicker neutron skin. This is correlated with the fact that the surface energy is lower within the nucleation calculation than within the harmonic oscillator method. Within the same numerical prescription, the neutron skin thickness is smaller with the TW model than with the NL3. As the coupling strength Λ_v increases in the NL$\omega\rho$ model, the results move from the original NL3 to the TW results for all quantities, except the proton radius, which oscillates a little. We have also included the results obtained with the HS parametrization [44] because we have used this parametrization in order to compare the TF and the Dirac results for the cross sections, as discussed in the following. As this parametrization is known not to give as good results as the other parametrizations of the NLWM for finite nuclei, we do not comment on the results it provides. Notice that the experimental radius for the protons is obtained from the charge radius R_c and it is given by $R_p = \sqrt{R_c^2 - 0.64}$ in fm [39]. Our results can be compared with experimental and other theoretical results found in the literature. The proton radius, which is known to better than 0.001 fm is better described within the TW model. This quantity is practically independent of the $\omega - \rho$ interaction strength in the NL$\omega\rho$ model as far as the HO numerical prescription is used. The neutron radius, on the other had, is strongly model dependent with drastic consequences in the neutron skin thickness calculation. The experimental values for θ are still very uncertain and all our results fall inside the experimental confidence interval. We shall comment on possible restrictions to the neutron skin thickness in the next section. NL3 provides the best results for the binding energy.

In [25], the results shown for the proton and neutron radius are respectively 5.52 and 5.85 fm, yielding a skin of 0.33 fm, larger than ours. Notice, however, that in [25] the Dirac equation was explicity solved. In [4], the authors obtained a value of 0.21 fm for the neutron skin thickness and a binding energy of -7.89 MeV within a different parametrization of the NL$\omega\rho$ model. Again in this case the Dirac equation was solved.

In Fig. 2 we show the difference between neutron and proton densities at the *Pb* surface for the models discussed in the present work with the Thomas-Fermi approximation solved in a harmonic oscillator basis. While the curves deviate a little in between 6.0 and 8.0 fm, at the very surface they are similar, but a small discrepancy, reflecting the differences in the neutron skin can be seen.

In Fig. 3 we display again the difference between neutron and proton densities within both numerical calculations of the TW and NL3 models. These two Thomas-Fermi calculations should have given more similar results. However the nucleation method predicts a very small surface energy for the NL3 parametrization, and therefore, a large radius. This may be related to the choice of the boundary conditions and a deeper comparison between the two methods will be pursued.

Next we present our results for the asymmetry given by eq. (47) as a function of the transfered momentum. We begin with Fig.4 which displays the results for the HS parametrization of the Walecka model. The curve labeled *no structure* means the case where $Z\rho_n(r) = N\rho_p(r)$ and the other two curves are obtained within the TF approximation and the full solution of the Dirac equation in

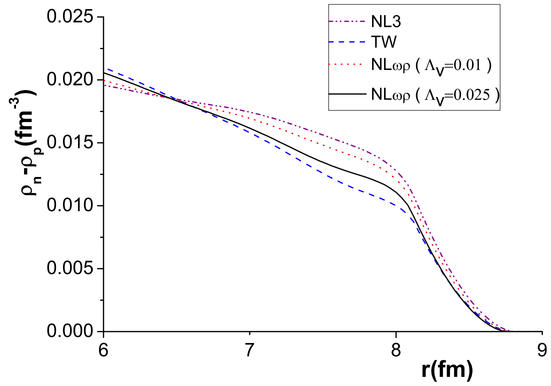

FIG. 2: Difference between neutron and proton densities obtained with the Thomas-Fermi approach solved in a harmonic oscillator basis for the models discussed in the present work.

the Hartree approximation. At the momentum transfer values of recent experimental interest (around $\simeq 0.4$ fm^{-1}), the curves are almost identical. A careful analysis of the same results in a different scale shows us that the asymmetry changes 12 and 11 percent respectively within the Dirac and TF approximations in comparison with the *no structure* case. Since it is the measurement of the asymmetry in this low momentum transfer region that will provide the accurate result for the neutron skin thickness, we have restricted our calculations to the TF approximation, as stated in the Introduction.

In Fig. 5a we show the asymmetry obtained with the NL3 model for both numerical calculations in the TF approximation, i.e, nucleation and HO expansion methods. In this case, the agreement is very satisfactory even for larger q-values, although the small numerical discrepancies is reflected in a ~ 10 percent difference in the predicted neutron skin thickness, as can be seen from Table II. Finally, in Fig. 5b our results for the NL$\omega\rho$ (using two different values for the $\omega - \rho$ coupling constant) and the TW models within the HO numerical prescription are shown. Again, at low momentum transfers, all curves coincide. However, it should be noticed that even for two different model parametrizations which lead us to identical neutron skin thicknesses, a measurement of the asymmetry in a higher q-region with a modest experimental precision, can distinguish between them. Also, we should expect that the asymmetry presents more structure in this high momentum transfer region if we solve the Dirac equation instead of using the TF approach, once the high q value region is much more sensitive to the central part of the neutron distribution, which is known to be *flat* in the TF approximation. These differences can be seen in Fig.4.

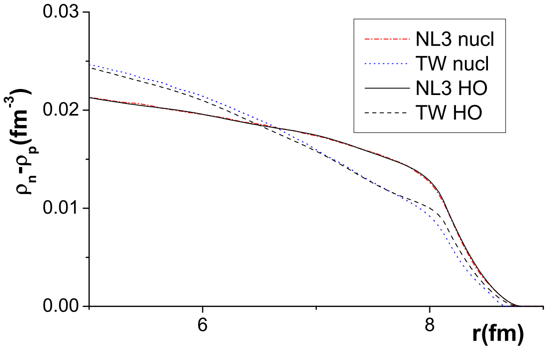

FIG. 3: Difference between neutron and proton densities obtained with the Thomas-Fermi approach solved with both numerical prescriptions for the TW model.

VII. DIFFERENT EOS, DIFFERENT NEUTRON SKINS

For the sake of completeness, at this point, we discuss some of the differences between the TW, the NL$\omega\rho$ models and the NL3 parametrization of the NLWM.
From Fig. 1 one can see that the largest possible pressure for a phase coexistence in the TW model is much lower, and appears at a lower proton fraction than the NL3 model. This gives rise to a thinner crust within the TW model, which may imply that the more exotic *pasta* shapes will not form [5]. The NL$\omega\rho$ model goes on a different direction, i.e., the pressure becomes higher than the one obtained with the NL3 as the Λ_v coupling is turned on.

Although the nuclear matter properties fitted to parametrize the models are quite similar (see Table I), the way the EoS behaves when extrapolated to higher or lower densities can vary a lot from a density dependent hadron model to one of the parametrizations of the NLWM. Moreover, as seen from Table I, although the effective mass at saturation density is lower with the TW than with the NL3, it can accommodate hyperons if an EoS for stellar matter is necessary, contrary to the usual

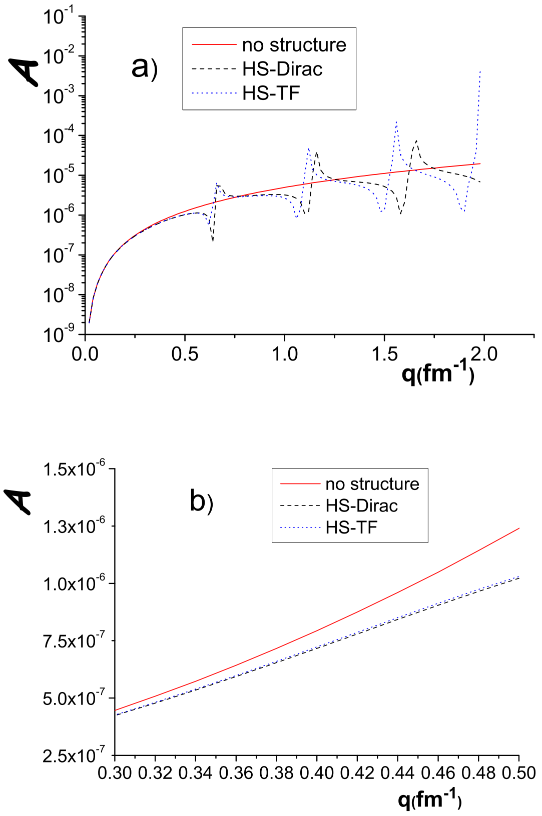

FIG. 4: Parametrization HS, comparison Thomas-Fermi-HO versus Dirac-HO

NL3 parametrization [32, 33, 34].

TABLE I: Nuclear matter properties.

	NL3	NL$\omega\rho$			TW
	[25]	[36]			[24]
		$\Lambda_v = 0.01$	$\Lambda_v = 0.02$	$\Lambda_v = 0.025$	
B/A (MeV)	16.3	16.3	16.3	16.3	16.3
ρ_0 (fm^{-3})	0.148	0.148	0.148	0.148	0.153
K (MeV)	271	271	271	271	240
$\mathcal{E}_{sym.}$ (MeV)	37.4	34.9	33.1	32.3	32.0
M^*/M	0.60	0.60	0.60	0.60	0.56
L (MeV)	118	88	68	61	55
K_{sym} (MeV)	100	-46	-53	-34	-124

Another quantity of interest in asymmetric nuclear matter is the nuclear bulk symmetry energy, shown in Table I for the saturation point. The differences in the symmetry energy at densities larger than the nuclear saturation density is still not well established, but has already been extensively discussed in the literature even for the TW model [7, 8, 16, 32]. Again, for the sake of completeness we reproduce these results here because the neutron skin thickness and the neutron star EoS are related by this quantity [1, 2, 3, 4], which is usually defined as $\mathcal{E}_{sym} = \frac{1}{2}\frac{\partial^2 \mathcal{E}/\rho}{\partial \delta^2}\Big|_{\delta=0}$, with $\delta = -\rho_3/\rho = 1 - 2y_p$. The symmetry energy can be analytically rewritten as

$$\mathcal{E}_{sym} = \frac{k_F^2}{6\epsilon_F} + \frac{\Gamma_\rho^2}{8m_\rho^2}\rho, \qquad (52)$$

for the TW model and as

$$\mathcal{E}_{sym} = \frac{k_F^2}{6\epsilon_F} + \frac{g_\rho^2}{8m_\rho^{*2}}\rho \qquad (53)$$

with the effective ρ-meson mass defined as [3]

$$m_\rho^{*2} = m_\rho^2 + 2g_v^2 g_\rho^2 \Lambda_v V_0^2$$

for the NL$\omega\rho$ model. In both cases

$$k_{Fp} = k_F(1+\delta)^{1/3}, \qquad k_{Fn} = k_F(1-\delta)^{1/3},$$

with $k_F = (1.5\pi^2\rho)^{1/3}$ and $\epsilon_F = \sqrt{k_F^2 + M^{*2}}$. In equations (52) and (53) the second term dominates at large densities. It is seen that the non-linear $\rho - \omega$ terms introduce a non-linear density behavior in the symmetry energy of the NLWM parametrizations such as NL3 and TM1. In TW the non-linear density behavior enters through the density dependent coupling parameters. These non-linear density behavior is important because the linear behavior of NL3 and TM1 parametrizations predicts too high symmetry energy at densities of importance for neutron star matter which has direct influence on the proton fraction dependence with density. From Fig. 6, it is easily seen that the symmetry energy obtained with the TW model behaves in a very different way, as compared with NL3. In [4] a relation between the symmetry energy and the nuclear binding energy is discussed : the harder the EoS, the more the symmetry

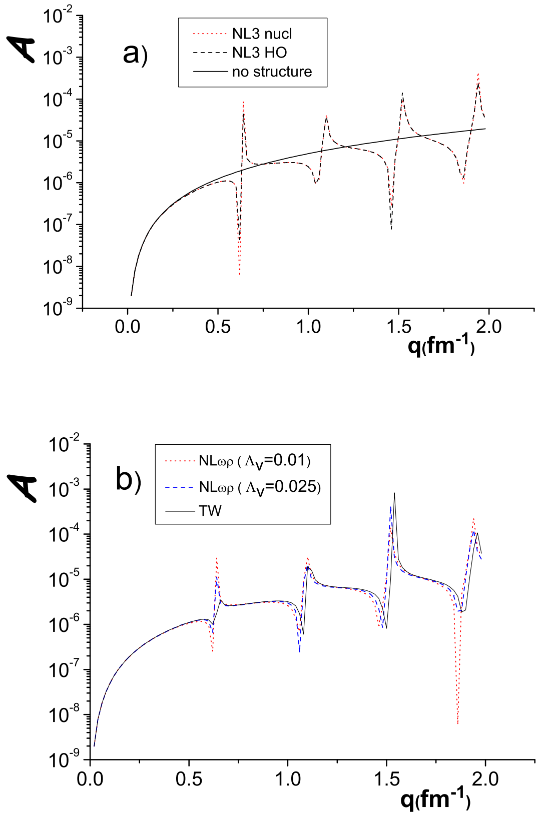

FIG. 5: Asymmetry obtained with a) NL3 with both numerical prescriptions and b)parametrizations NL$\omega\rho$ and TW

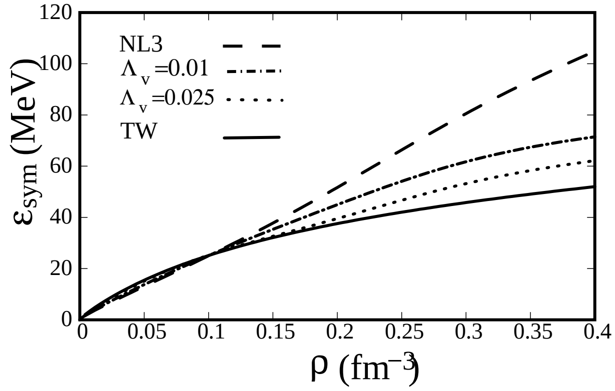

FIG. 6: Symmetry energy for the NL3, TW and NL$\omega\rho$ models.

energy rises with density. The density dependence discussed in [4] is of the type introduced in [3, 36] through the inclusion of a $\sigma-\rho$ and/or $\omega-\rho$ couplings and then, similar with the NL$\omega\rho$ model discussed here. One can observe that as the strength of the coupling increases, the symmetry energy gets closer to the TW curve. In fact, in [8] it was shown that once this kind of coupling is introduced with a reasonable strength, the symmetry energy at low densities tends to behave as the TW model.

The symmetry energy can be expanded around the nuclear saturation density and reads

$$\mathcal{E}_{sym}(\rho) = \mathcal{E}_{sym}(\rho_0) + \frac{L}{3}\left(\frac{\rho-\rho_0}{\rho_0}\right) + \frac{K_{sym}}{18}\left(\frac{\rho-\rho_0}{\rho_0}\right)^2, \tag{54}$$

where L and K_{sym} are respectively the slope and the curvature of the nuclear symmetry energy at ρ_0 and they are calculated from

$$L = 3\rho_0 \frac{\partial \mathcal{E}_{sym}(\rho)}{\partial \rho}|_{\rho=\rho_0} \quad K_{sym} = 9\rho_0^2 \frac{\partial^2 \mathcal{E}_{sym}(\rho)}{\partial^2 \rho}|_{\rho=\rho_0}. \tag{55}$$

These two quantities can provide important information on the symmetry energy at both high and low densities because they characterize the density dependence of the energy symmetry. In a recent work [49], the authors found a correlation between the slope of the symmetry energy and the neutron skin thickness. In their work 21 sets of the non-relativistic Skyrme potential were investigated and only 4 of them were shown to have L values consistent with the values extracted from experimental isospin diffusion data from heavy ion collisions. In fact, the extracted value was $L = 88 \pm 25$ MeV [50], which gives a very strong constraint on the density dependence of the nuclear symmetry energy and consequently on the EoS as well. A detailed analysis of Table I shows that, if this constraint is to be taken seriously, neither the NL3 nor the TW model satisfy it. Nevertheless, the NL$\omega\rho$ slope interpolates beautifully between the NL3 and TW slope values. Once again it is seen that the increase in Λ_v approximates the NL3 model values for the slope and energy symmetry to the TW values. Moreover, we have also tried to find a correlation between the θ values shown in Table II and L values displayed in Table I. We found that, as far as some numerical imprecision are considered, larger values of L correspond to larger values of the neutron skin, as seen in Fig. 7.

Let's now go back to the problem of solving the differential equations within the nucleation numerical prescription. As we need boundary conditions arising from the liquid-gas phase coexistence in order to solve eqs. (12-15) for the TW model and eqs. (22-25) for the NL$\omega\rho$ model, the binodal sections are essential and the spinodal sections, which separate the regions of stable to unstable matter are also of interest. If we had displayed the binodals in a ρ_p versus ρ_n plot, as it is done with the spinodals in Fig 8, we could see that the spinodals surfaces lie inside the binodal sections and share the critical point corresponding to the highest pressure.

In Fig. 8 the spinodals for the three different models discussed in this work are shown. Once again, some of these results can also be found in the recent literature [7, 8], but we include them here to make a direct link with the binodals. The instability of the ANM system is essentially determined by density fluctuations in the isoscalar channel. Although the spinodals are, by themselves, not relevant in calculations performed at the thermodynamical equilibrium, the isospin channel is very sensitive to the instabilities occurring below the nuclear saturation density. The spinodal is determined by the values of pressure, proton fraction and density for which the determinant of

$$\mathcal{F}_{ij} = \left(\frac{\partial^2 \mathcal{F}}{\partial \rho_i \partial \rho_j}\right)_T, \tag{56}$$

where $\mathcal{F}$ is the free energy density, goes to zero. A detailed analysis of this quantity can be found in [8, 42]. From Fig. 8, it is seen that the instability region in the ρ_p/ρ_n plane, defined by the inner section of the spinodal curve is larger for the TW than for the NL3 model. The size of the instability region depends on the derivative of the chemical potentials with respect to the neutron and proton densities. At low densities different models exhibit different behaviors.

The presence of the rearrangement term in the TW model also plays a decisive role. Even though a relatively large compensation exists between scalar and vector mesons in the isoscalar channels within the rearrangement term at low densities, the spinodal region is defined by the derivative of the chemical potential and therefore of the rearrangement term.

Next we examine the spinodals obtained with different coupling strengths for the NL$\omega\rho$ model. As seen in Fig. 8, there is almost no difference between the different curves. They all fall around the original NL3 curve but once again, they tend to the TW curve as the coupling strength increases. However, contrary to the TW model, it was shown in [9] that the direction of the instability in

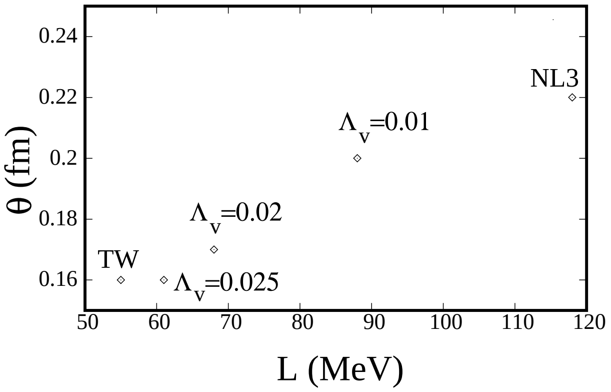

FIG. 7: Correlation between the neutron skin θ and the slope of the symmetry energy L.

$\mathrm{NL}_{\omega\rho}$ increases distillation as the density increases, and the larger the coupling Λ_v the larger the effect.

Finally, to end this section, let's make our points clear: we have used a simple mean field theory approach to obtain the boundary conditions for the equations of motion of the meson fields in the nucleation prescription. These boundary conditions depend on the model used and are intrinsically related with the liquid-gas phase transition which, in turn, can be well understood by studying the coexistence surfaces of the corresponding models. On the other hand, the neutron skin thickness shows a linear correlation with the slope of the symmetry energy, as already pointed out in [49] for non-relativistic models. Based on the different behaviors found with density dependent hadronic models and the NLWM, an obvious consequence is the fact that the neutron skin thickness depends on the choice of the model.

VIII. CONCLUSIONS

We have calculated the ^{208}Pb neutron skin thickness with two different density dependent hadronic models, the TW and the NL$\omega\rho$ model, and one of the most used parametrizations of the NLWM, the NL3. The calculations were done within the Thomas-Fermi approximation, which gives quite accurate results for the asymmetry in the momentum transfer range of interest for the calculation of neutron skins. In implementing the numerical results two different prescriptions were used: the first one based on the nucleation process and the second one based on the harmonic oscillator basis method. We have seen that when the nucleation method is performed, the neutron radius is systematically larger, what results in a thicker neutron skin. This is a consequence of the fact that the surface energy is lower within the nucleation calculation than within the harmonic oscillator method. Within the same numerical prescription, the neutron skin thickness is smaller with the TW model than with the NL3. As the coupling strength Λ_v increases in the NL$\omega\rho$ model, the neutron skin thickness moves from the original NL3 towards the TW results. We have also found that although the neutron skin thickness is model dependent, the asymmetry at low momentum transfers (below 0.5 fm^{-1}) is very similar for all models and all numerical prescriptions. As q increases, the asymmetry also becomes model dependent. The density profiles obtained from the solution of the Dirac equation exhibits oscillations near the center of the nucleus, behavior which is not reproduced within the Thomas-Fermi approximation. This fact shows up in the asymmetry at large momentum transfers and therefore all the calculations should be reproduced by solving the Dirac equation. This calculation is already under investigation.

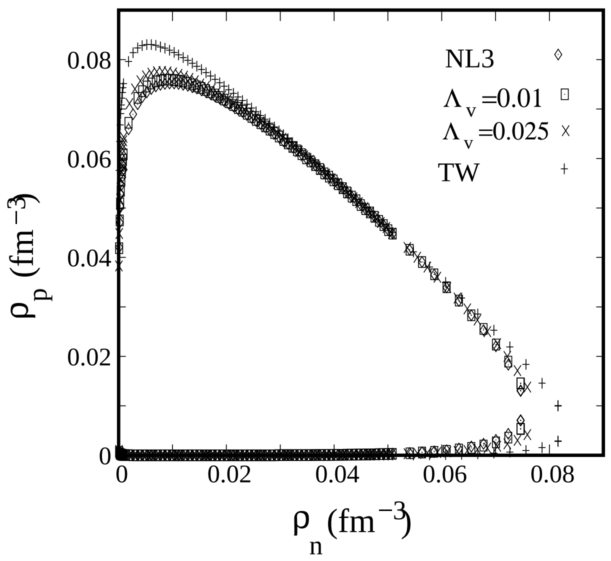

FIG. 8: Spinodal section in terms of ρ_p versus ρ_n for the NL3, TW and NL$\omega\rho$ models.

It is worth mentioning that the neutron skin thickness has shown to give hints on the equations of state that are suitable to describe neutron stars. Moreover, in [49] a correlation between the slope of the symmetry energy and the neutron skin thickness was found for Skyrme-type models. We have observed that this correlation was also present in the density dependent models we have studied in the present work.

ACKNOWLEDGMENTS

This work was partially supported by CNPq(Brazil), CAPES(Brazil)/GRICES (Portugal) under project 100/03 and FEDER/FCT (Portugal) under the projects POCTI/FP/63419/2005 and POCTI/FP/63918/2005.

---

[1] S. Typel and B.A. Brown, Phys. Rev. **C 64**, 027302 (2001).

[2] A.W. Steiner, M. Prakash, J.M. Lattimer and P.J. Ellis, Phys. Rep. **411**, 325 (2005).

[3] C.J. Horowitz and J.Piekarewicz, Phys. Rev. Lett. **86**, 5647 (2001).

[4] J.Piekarewicz, nucl-th/0607039. Proceedings of the "International Conference on Current Problems in Nuclear Physics and Atomic Energy" (May 29 - June 3, 2006) Kyiv, UKRAINE.

[5] F. Duchoin and Haensel, Phys. Lett. **B 485**, 107 (2000).

[6] Ph. Chomaz, C. Colonna and J. Randrup, Phys. Rep. **389**, 263 (2004).

[7] S.S. Avancini, L. Brito, D. P. Menezes and C. Providência, Phys. Rev. **C 70**, 015203 (2004).

[8] S.S. Avancini, L. Brito, Ph. Chomaz, D. P. Menezes and C. Providência, Phys. Rev. **C 74**, 024317 (2006).

[9] C. Providência, L. Brito, S.S. Avancini, D. P. Menezes and Ph. Chomaz, Phys. Rev. **C 73**, 025805 (2006).

[10] L. Brito, C. Providência, A.M.S. Santos, S.S. Avancini, D. P. Menezes and Ph. Chomaz. Phys. Rev. **C** (2006), **C 74**, 045801 (2006); C. Providência, L. Brito, A.M.S. Santos, D.P. Menezes and S.S. Avancini, Phys. Rev. **C 74**, 045802 (2006).

[11] Ph. Chomaz and F. Gulminelli, Phys. Lett. **B447**, 221 (1999) 221; H. S. Xu, *et al*, Phys. Rev. Lett. **85**, 716 (2000).

[12] C. Ducoin, Ph. Chomaz and F. Gulminelli, Nucl. Phys. **771**, 68 (2006).

[13] Ph. Chomaz, Nucl. Phys. **A 685**, 274c (2001).

[14] E. Chabanat, P. Bonche, P. Haensel, J. Meyer and R. Schaeffer, Nucl. Phys. **A 627**, 710 (1997).

[15] C. Providência, D. P. Menezes, L. Brito and Ph. Chomaz, in preparation.

[16] B.A. Li, C.M. Ko and W. Bauer, Inter. J. Mod. Phys. **E 7**, 147 (1998).

[17] K. Pomorski, P. Ring, G.A. Lalazissis, A. Baran, Z. Lojewski, B. Nerlo-Pomorska, M. Warda, Nucl. Phys. **A 624**, 349 (1997).

[18] D. G. Ravenhall, C. J. Pethick, and J. R. Wilson, Phys. Rev. Lett. **50**, 2066 (1983); M. Hashimoto, H. Seki, and M. Yamada, Prog. Theor. Phys.**71**, 320 (1984).

[19] H. de Vries, C.W. de Jager and C. de Vries, Atomic and Nuclear Data Tables **36**, 495 (1987).

[20] C.J. Horowitz, S.J. Pollock, P.A. Souder and R. Michaels, Phys. Rev. **C 63**, 025501 (2001).

[21] T.W. Donnelly, J. Dubach and I. Sick, Nucl. Phys. **A503** 589 (1989).

[22] K.A. Aniol et al. (HAPPEX) (2005), nucl-ex/0506010; *ibidem*, nucl-ex/0506011; R. Michaels, P.A. Souder and G.M. Urciuoli (2005), URL http://hallaweb.jlab.org/parity/prex.

[23] H. Lenske and C. Fuchs, Phys. Lett. **B 345**, 355 (1995); C. Fuchs, H. Lenske and H.H. Wolter, Phys. Rev. **C 52**, 3043 (1995).

[24] S. Typel and H. H. Wolter, Nucl. Phys. **A656**, 331 (1999).

[25] G. A. Lalazissis, J. König and P. Ring, Phys. Rev. C **55**, 540 (1997).

[26] K. Sumiyoshi, H. Kuwabara, H. Toki, Nucl. Phys. **A 581**, 725 (1995).

[27] C. Fuchs, H. Lenske and H.H. Wolter, Phys. Rev. **C 52**, 3043 (1995).

[28] H. Lenske and C. Fuchs, Phys. Lett. **B 345**, 355 (1995).

[29] B. ter Haar and R. Malfliet, Phys. Rep. **149**, 207 (1987).

[30] T. Nikšić, D. Vretenar, P. Finelli and P. Ring, Phys. Rev. **C 66**, 024303 (2002).

[31] B. Serot and J.D. Walecka, *Advances in Nuclear Physics* 16, Plenum-Press, (1986) 1.

[32] S.S. Avancini and D.P. Menezes, Phys. Rev. **C 74**, 015201 (2006).

[33] D.P. Menezes and C. Providência, Phys. Rev. **C 68**, 035804 (2003); Braz. J. Phys. **34**, 724 (2004).

[34] A.M.S. Santos and D.P. Menezes, Phys. Rev. **C 69**, 045803 (2004).

[35] C.J. Horowitz and J.Piekarewicz, Phys. Rev.**C 64**, 062802 (2001).

[36] J.K. Bunta and S. Gmuca, Phys. Rev. C **68**, 054318 (2003).

[37] J.K. Bunta and S. Gmuca, Phys. Rev. C **70**, 054309 (2004).

[38] D.P. Menezes and C. Providência, Nucl. Phys. **A 650**, 283 (1999); D.P. Menezes and C. Providência, Phys. Rev. **C 60**, 024313 (1999); D.P. Menezes and C. Providência, Phys. Rev. **C 64**, 044306 (2001).

[39] Y.K. Gambhir, P. Ring and A. Thimet, Ann. Phys. **198**, 132 (1990).

[40] T. Gaitanos, M. Di Toro, S. Typel, V. Baran, C. Fuchs, V. Greco and H. H. Wolter, Nucl. Phys. **A 732**, 24 (2004).

[41] S.S. Avancini, M.E. Bracco, M. Chiapparini and D.P. Menezes, J. Phys. G **30**, 27 (2004); S.S. Avancini, M.E. Bracco, M. Chiapparini and D.P. Menezes, Phys. Rev. **C 67**, 024301 (2003).

[42] J. Margueron and P. Chomaz, Phys. Rev. C **67**, 041602 (2003).

[43] C.J. Horowitz, Phys. Rev. **C57**, 3430 (1998).

[44] C.J. Horowitz and B.D. Serot, Nucl. Phys. **A 368**, 503 (1981).

[45] G.Fricke, C. Bernhardt, K.Heilig, L.A. Schaller, L. Schellinberg, E.B. Shera,C.W. de Jager, At. Data Nucl. Data Tables **60** (1995)177.

[46] G. Audi, A.H. Waptra, C. Thibault, Nucl. Phys. **A 729**, 337 (2003).

[47] A. Krasznahorkay et a., Nucl. Phys. **A 731**, 224 (2004).

[48] V.E. Starodubsky, N.M. Hintz,Phys. Rev. **C49**,2118(1994).

[49] L. Chen, C.M. Ko and B. Li, nucl-th/0610057.

[50] M.B. Tsang et al., Phys. Rev. Lett. **92**, 062701 (2004).

TABLE II: ^{208} Pb properties

model	approximation	R_n (fm)	R_p (fm)	θ (fm)	B/A MeV	σ Mev/fm^2
NL3	TF+nucleation	5.88	5.65	0.24	-7.77	0.76
NL3	TF+HO	5.79	5.57	0.22	-7.79	0.96
NL$\omega\rho$, $\Lambda_v = 0.01$	TF+HO	5.77	5.57	0.20	-7.73	0.98
NL$\omega\rho$, $\Lambda_v = 0.02$	TF+HO	5.75	5.57	0.17	-7.65	0.99
NL$\omega\rho$, $\Lambda_v = 0.025$	TF+HO	5.74	5.58	0.16	-7.63	1.00
TW	TF+nucleation	5.71	5.50	0.22	-6.42	1.08
TW	TF+HO	5.68	5.52	0.16	-7.46	1.10
HS	TF+HO	5.70	5.47	0.24	-6.10	1.37
exp.[45]			5.44			
exp. [46]					-7.87	
exp. [47]				0.12 ± 0.07		
exp. [48]				0.20 ± 0.04		